




Shahid Chamran  
University of Ahvaz

# Journal of Applied and Computational Mechanics



Research Paper

## Efficacy of a Modulated Viscosity-dependent Temperature/nanoparticles Concentration Parameter on a Nonlinear Radiative Electromagneto-nanofluid Flow along an Elongated Stretching Sheet

Ji-Huan He<sup>1,2,3</sup> , Nasser S. Elgazery<sup>4</sup> , Khaled Elagamy<sup>4</sup> , Nader Y. Abd Elazem<sup>5</sup> 

<sup>1</sup> National Engineering Laboratory for Modern Silk, College of Textile and Clothing Engineering, Soochow University, Suzhou, China

<sup>2</sup> School of Mathematics and Information Science, Henan Polytechnic University, Jiaozuo, China

<sup>3</sup> School of Science, Xi'an University of Architecture and Technology, China, Email: hejihuan@suda.edu.cn

<sup>4</sup> Department of Mathematics, Faculty of Education, Ain Shams University, El-Makrizy St, Roxy, Heliopolis, Cairo, Egypt, Email: nasersaleh@edu.asu.edu.eg (N.S.E.), Khaledelagamy2004@gmail.com (K.E.)

<sup>5</sup> Department of Basic Science, Cairo Higher Institute for Engineering, Computer Science and Management, New Cairo, Cairo, Egypt, Email: naderelnafrawy@yahoo.com; nader\_47@hotmail.com

Received November 10 2022; Revised January 07 2023; Accepted for publication January 29 2023.

Corresponding author: J.H. He (hejihuan@suda.edu.cn)

© 2023 Published by Shahid Chamran University of Ahvaz

**Abstract.** The purpose of the present communication is to investigate the flow of a radiative electromagnetic-Casson nanofluid past a stretching sheet under the impacts of a chemical reaction and nonlinear thermal radiation. To enrich the blood flow, a modulated viscosity/thermal conductivity dependent temperature/nanoparticles concentration parameter is included in the governing equations. The system of PDEs is transformed to ODEs by invoking similarity transformations and then solved numerically by the well-known fourth-order Runge-Kutta integration scheme based on shooting approach. The main factors affecting the Casson fluid's temperature profiles are revealed.

**Keywords:** Stretching sheet; Electromagnetic Casson nanofluid; Nonlinear radiation; Variable viscosity/thermal conductivity; Shooting technique.

### 1. Introduction

Nanofluids are defined as the fluids containing nanoscale particles. Where the nanoparticles have highly thermal conductivity, then adding nanoparticles to the main liquid raises the thermal conductivity of the out coming combination. Although the previous studies were concerned with examining the physical properties of conventional heat transfer through liquids, recently, with the interest in the discussion of nanofluids, the present investigations have become so effective as well as capable of meeting modern technology. Therefore, the inspection of nanofluids can play an essential role in numerous industrial, engineering, physical, and chemical applications. For example, hybrid engines, producing high-quality lubricants oil, nano-biofuel cells, microelectronics, etc. [1, 2].

The non-Newtonian fluid behavior of a lot of industrial fluids is known via a shear-dependent viscosity. Where, the shear rate is not proportional to the shear stress directly. Therefore, the study of non-Newtonian fluids flow attracted the interest of many scientists for its various engineering as well as manufacturing applications such as: food processing (ice flows, chocolates, ketchup, sauces, magma, condensed milk), biological materials (vacancies, synovial liquid, animal blood), chemical materials (slurries, molten plastics, polymer liquids, polymer extrusion, drilling mud, petroleum products, shampoos, paints, detergents, pharmaceutical chemicals) and etc. In recent years, plentiful of non-Newtonian models have been introduced as an expression of the rheological properties of several kinds of fluids. Furthermore, the physiological fluids in the human body have been considered as non-Newtonian fluid. Human blood consists of plasma (platelets in a complex solution 90% water), white blood cells (leukocytes), red blood cells (erythrocytes), lipids, carbohydrates, proteins, fibrinogen, salts, and gases. Commonly the human blood can be treated as a non-Newtonian fluid made up of blood cells and plasma [3-5].

The Casson model is one of the famous non-Newtonian fluids models. In 1959, Casson [6] first introduced this model to predict the flow behavior of dye-oil suspension. Recently, this model has several features as well as is so renowned which characterized by high shear viscosity and yield stress. This model is based on a structure model of the composite manner of liquid and solid phases of two-phase suspensions. So that, Casson model can represent the purely viscous fluid which have high viscosity such as



concentrated fruit juice, soup, honey, tomato sauce, ink, and jelly. In addition, the human blood can be treated as Casson fluid due to the existence of sundry substances, where, the internal friction (viscosity) of blood raises with rising the percentage of red cells inside the blood, more red cells mean greater viscosity, which means a more friction. Therefore, the Casson fluid has various applications in blood cells, fibrinogen, and cancer therapy. On the other hand, for the flow, the Casson fluid is transformed to a rigid body if the yield shear stress is greater than the shear stress. Moreover, the yield stress of Casson fluid needs to exceed the shear stress, or else the fluid behaves as a Newtonian fluid [7]. As a result, many researchers are motivated by heat transfer for Casson fluid flow from a variety of physical perspectives. Walawender et al. [8] used an approximate Casson fluid model for studying a blood flow in tube. Furthermore, the blood flow with peristaltic transport using the Casson model has been introduced by Srivastava and Srivastava [9]. Dash et al. [10] studied the Casson fluid flow through a pipe with a porous medium. A MHD Casson fluid flow between two rotating cylinders is studied by Eldabe et al. [11]. Moreover, Mernone et al. [12] suggested a mathematical investigation of peristaltic transport using the Casson fluid model. An unsteady Casson fluid flow over a moving flat sheet is investigated by Mustafa et al. [13]. Shehzad et al. [14] tested a MHD of Casson fluid flow with mass transfer under the effects of suction and chemical reaction. The study of the Casson fluid flow with nanoparticles has been introduced by Hayat et al. [15]. Furthermore, Gireesha et al. [7] employed the Runge-Kutta based shooting technique to obtain a numerical solution for the Casson-Carreau fluid flow with homogeneous – heterogeneous reactions. The effect of nonlinear thermal radiation on a MHD Casson nanofluid flow in the existence of Joule heating past an inclined porous stretching plate is investigated by Ghadikolaei et al. [16]. Aman et al. [17] evaluated an exact solutions for MHD hybrid Casson-nanofluid flow under the impact of porosity. After that, utilizing the finite-difference numerical method Siddiqua et al. [18] have been inspected a dusty radiative Casson fluid flow near a wavy plate surface. They found that, in the presence of mass concentration and radiation parameters the rate of heat transfer raises extensively. In order to examine a magneto blood flow with alumina and gold nanoparticles into a porous medium, Elgazery [19] applied the Chebyshev pseudospectral (CPS) technique. As well as, a numerical analysis via the implicit finite-difference approach for an unsteady natural convection of a dusty Casson fluid flow past a wavy surface has been given by Hady et al. [20]. By employing the Spectral quasi-linearization technique Akolade and Tijani [21] checked a comparative numerical study for Williamson-Casson nanofluid flow over a riga surface. This numerical study is found to be applicable in biomedical as well as engineering field. Also, as an application of bacterial growth along the heart valve, the nanoparticles through a MHD Casson nanofluid (blood) flow with slip effect has been tested in Ref. [22]. In the presence of couple stress an electromagnetic hybrid Casson nanofluid flow near an unsteady rotating disc has been checked by Usman et al. [23] via the homotopy analysis technique. Recently, Kumar et al. [24] introduced a modeling and theoretical study for a Casson nanofluid flow past near a curved stretching sheet under both chemical reaction and magnetic field impact. Also, the influence of Dufour and Soret on a MHD Casson fluid flow over a stretching plate in the presence of diffusive-convective conditions was studied by Ramudu et al. [25].

Due to the importance of changing the physical properties of the fluid with the temperature, many scientists have been excited to study the effect of these variable properties on the fluid flow in various cases. Elgazery and Hassan [26] and Elgazery and El-Sayed [27] checked the impact of variable fluid properties on a magneto-Casson fluid flow over a stretching plate through a porous medium. Elgazery [28] presented also another numerical investigation for a Casson fluid flow under the influence of the variable properties. Moreover, the impacts of chemical reaction as well as thermophoresis on free convective mass and heat transfer of a magneto-dissipative Casson fluid flow in the presence of variable viscosity/thermal conductivity have been examined by Animasaun [29]. El-Aziz and Afify [30] tested the heat transfer and MHD unsteady Casson fluid film flow along a stretching sheet under the impacts of both thermal radiation and variable thermal conductivity. Furthermore, an axisymmetric MHD Casson fluid flow with variable thermal conductivity is inspected by Nawaz et al. [31]. Recently, Sohail et al. [32] applied the optimal homotopy analysis technique to calculate an analytical solution for a MHD Casson fluid flow with entropy generation under the influence of variable thermal conductivity and heat conductance past a bi-directional non-linear stretching sheet. By utilizing the implicit finite difference approach, Bisht and Sharma [33] are obtained a numerical solution for an impact of both variable viscosity and thermal conductivity on a Casson nanofluid flow over a non-linear stretching surface. They noticed that, with an increase in the viscosity variation parameter, the velocity distribution raises whereas with an increase in the Casson parameter it decreases. Further, Khaled and Khan [1] introduced a vital study applicable in bio-technology for gyrotactic microorganisms swimming in a Casson nanofluid under the effects of variable viscosity and thermal conductivity. The thermal aspects for variable thermal conductivity and viscosity on a Casson nanofluid flow with velocity slip and convective heating are investigated by Gbadeyan et al. [2]. Also, as an application in the transdermal drug delivery, Elgazery and Elelmy [34] has been tested the variable thermal conductivity influence on a Casson nanofluid flow along a stretching plate in the presence of a nonlinear thermal radiation. They observed that, although the linear radiation has a weak impact on the concentration profiles of nanoparticles, these profiles distributions are highly effected by the nonlinear thermal radiation. For more recently studies see also [35, 36].

By taking into count the efforts of the past scientists, the current work focuses on the detailed investigation of a radiative electromagneto- Casson nanofluid flow past a stretching sheet under the impacts of chemical reaction and nonlinear thermal radiation by considering a modulated viscosity as well as thermal conductivity dependent temperature and nanoparticles concentration. The arising system for the physical model is solved numerically by well-known shooting method with Runge-Kutta fourth-order technique. The behavior of all important physical parameters is illustrated graphically as well as tabular with a suitable discussion. In order to show a good presentation, the current paper is divided as follows: Section 2 is devoted to formulate a PDEs system which governs the physical problem. The numerical approach of the governing mathematical system is given in Section 3. An appropriate discussion for the numerical results has been incorporated in Section 4. The conclusion part has been written in the last section.

## 2. Mathematical Formulations

In this section, a steady incompressible two-dimensional radiative electromagneto-Casson nanofluid flow past through a stretching sheet has been proposed. Nonlinear thermal radiation and homogeneous chemical reactions with first order influences have also been included. The horizontal sheet is thought to be preserved when the temperature  $T_w$  and nanoparticle concentration  $C_w$  are higher than the ambient temperature  $T_\infty$  and nanoparticle concentration  $C_\infty$ . The  $(x,y)$ -coordinate system is used, with the horizontal  $x$ -axis representing the stretching sheet and the vertical  $y$ -axis representing the normal to the stretching sheet. The zone  $y > 0$  is occupied by nanofluid flow in this study. When the current fluid is electrically conducting, the Lorenz force is calculated as  $J \times B$ . The electrical conducting density  $J = \sigma(E + V \times B)$  is represented here (joule current). Moreover,  $\sigma$  denotes the electrical conductivity and  $V = (u,v)$  are velocities of nanofluids in  $(x,y)$ - coordinates along and perpendicular to the surface [37].  $E = (0,0,-E_0)$  and  $B = (0,B_0,0)$  represent the uniform electric and magnetic field vectors of strength that are applied normally to the fluid flow. While the magnetic Reynolds number is chosen to be small. Figure 1 depicts the flow regime and coordinate system of the considered problem.



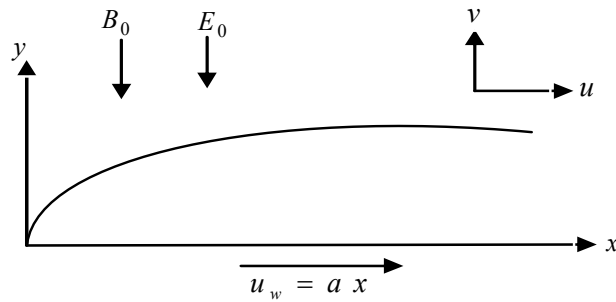


Fig. 1. The (x, y)-coordinate system and flow configuration.

The momentum equation now includes a stress tensor  $\tau_{ij}$  defined as [19, 22, 27, 28, 34]:

$$\tau_{ij} = \begin{cases} 2(\mu + p_y / \sqrt{2\pi_0}) e_{ij} & \pi_0 \geq \pi_c, \\ 2(\mu + p_y / \sqrt{2\pi_c}) e_{ij} & \pi_0 < \pi_c. \end{cases} \tag{1}$$

where  $p_y$  represents the yield stress as well as  $\mu$  represents the nanofluid effective plastic dynamic viscosity. It is clear that as  $p_y \rightarrow 0$ , the Casson model tends to the ordinary Newtonian model.  $\pi_c$  represents a critical value of the product  $\pi_0 = e_{ij}e_{ij}$ . Moreover,  $e_{ij}$  represents the  $(i, j)^{th}$  component of the deformation rate,  $e_{ij} = (\partial v_i / \partial x_j + \partial v_j / \partial x_i) / 2$ .

According to the constraints stated above, the fundamental system for momentum, mass conservation, concentration, and energy with Casson nanofluid flow is expressed as [20, 34, 38, 39]:

The equation of continuity:

$$\frac{\partial u}{\partial x} + \frac{\partial v}{\partial y} = 0 \tag{2}$$

The equation of momentum:

$$u \frac{\partial u}{\partial x} + v \frac{\partial u}{\partial y} = \frac{1}{\rho_f} \frac{\partial}{\partial y} \left[ \left( \mu(T, C) + \frac{p_y}{\sqrt{2\pi_c}} \right) \frac{\partial u}{\partial y} \right] + \frac{\sigma}{\rho_f} (E_0 B_0 - u B_0^2) \tag{3}$$

The equation of energy:

$$u \frac{\partial T}{\partial x} + v \frac{\partial T}{\partial y} = \frac{1}{(\rho c_p)_f} \frac{\partial}{\partial y} \left[ k(T, C) \frac{\partial T}{\partial y} \right] - \frac{1}{(\rho c_p)_f} \frac{\partial q_r}{\partial y} + \frac{\sigma (B_0 u - E_0)^2}{(\rho c_p)_f} + \Gamma \left( D_B \frac{\partial C}{\partial y} \frac{\partial T}{\partial y} + \frac{D_T}{T_\infty} \left( \frac{\partial T}{\partial y} \right)^2 \right) \tag{4}$$

The equation of concentration of nanoparticles:

$$u \frac{\partial C}{\partial x} + v \frac{\partial C}{\partial y} = \frac{D_T}{T_\infty} \frac{\partial^2 T}{\partial y^2} + D_B \frac{\partial^2 C}{\partial y^2} - R_c (C - C_\infty) \tag{5}$$

The boundary conditions in the above system are given by:

$$\begin{aligned} \text{at } y = 0: & \quad u = u_w = ax, \quad v = 0, \quad T = T_w, \quad C = C_w \\ \text{as } y \rightarrow \infty: & \quad u \rightarrow 0, \quad T \rightarrow T_\infty, \quad C \rightarrow C_\infty \end{aligned} \tag{6}$$

In the above system,  $T$  and  $C$  are the temperature, and nanoparticles concentration.  $c_p$ ,  $\rho_f$ ,  $D_T$  and  $D_B$  are the specific heat at constant pressure, nanofluid density, thermophoresis, and Brownian diffusion coefficients, respectively.  $(\rho c_p)_s$  and  $(\rho c_p)_f$  represent the effective heat capacity of the nanoparticles and the heat capacity of the fluid.  $\Gamma$  also represents the ratio  $(\rho c_p)_s / (\rho c_p)_f$ .  $R_c$  is the homogeneous chemical reaction and  $u_w = ax$  is the stretching velocity where  $a$  is constant. Also,  $q_r = -(4\sigma^* / 3\kappa)(\partial T^4 / \partial y)$  is the radiative heat flux, where  $\kappa$  and  $\sigma^*$  represent the mean absorption coefficient and the Stefan-Boltzmann constant. Therefore, the nonlinear thermal radiation term following by Elgazery and Elelamy [34] is given by  $\partial q_r / \partial y = -(16\sigma^* / 3\kappa)[3T^2(\partial T / \partial y) + T^3(\partial^2 T / \partial y^2)]$ .

In addition, in the most of previous literature, all properties of the fluid are assumed constant with temperature. Since this investigation is related to the inspection of the blood flow in the presence of nanoparticles under the nonlinear thermal radiation impact, it is significant to modify the nanofluid viscosity  $\mu$  and thermal conductivity  $k$  proportional to the nanofluid temperature and nanoparticles concentration as follows [34]:

$$\mu(T, C) = \mu_0 \exp[-\{q_1(T - T_\infty) + q_2 C_\infty\}] \tag{7}$$

$$k(T, C) = k_0 [1 + q_3(T - T_\infty)][1 + q_4 C_\infty] \tag{8}$$

where  $q_i$ ,  $i = 1, 2, 3, 4$  are dimensionless coefficients.  $\mu_0$  and  $k_0$  are the constant nanofluid viscosity and thermal conductivity, respectively.



Now using the next similarity transformation [34, 39]:

$$\eta = y\sqrt{a(\rho_f / \mu_0)}, \quad \psi = x f(\eta)\sqrt{a(\mu_0 / \rho_f)}, \quad u = \psi_x = a x f'(\eta), \quad v = -\psi_y = -f(\eta)\sqrt{a(\mu_0 / \rho_f)}, T - T_\infty = \Delta T \theta, C - C_\infty = \Delta C \phi \tag{9}$$

Here,  $\Delta T = (T_w - T_\infty)$  and  $\Delta C = (C_w - C_\infty)$  are the difference of temperature as well as nanoparticle concentration between the sheet and far field.  $\eta$  and  $\psi$  are the similarity variable and stream function. Further,  $f(\eta)$ ,  $\phi(\eta)$  and  $\theta(\eta)$  represent the dimensionless velocity, nanoparticle concentration and temperature functions, respectively.

The modification of both nanofluid viscosity as well as thermal conductivity with the dimensionless nanoparticle concentration and temperature functions are formed as following:

$$\mu(\theta, \phi) = \mu_0 \exp[-\{\beta_1 \theta(\eta) + \beta_2 \phi(\eta)\}] \tag{10}$$

$$k(\theta, \phi) = k_0 [1 + \beta_3 \theta(\eta)][1 + \beta_4 \phi(\eta)] \tag{11}$$

Here  $\beta_1 = q_1(T_w - T_\infty)$  and  $\beta_3 = q_3(T_w - T_\infty)$  represent the viscosity and thermal conductivity temperature variation parameters, respectively.  $\beta_2 = q_2(C_w - C_\infty)$  and  $\beta_4 = q_4(C_w - C_\infty)$  represent also the viscosity and thermal conductivity nanoparticles concentration variation parameters, respectively. Where the values of  $\beta_i$ ,  $i = 1, 2, 3, 4$  are related to the kind of nanofluid.

Then by using transformation (9) and utilizing the above modulation in the nanofluid viscosity and thermal conductivity, the system of PDFs (2)–(6) is rewritten by the following ODEs:

$$\frac{1}{\beta} f''''(\eta) - (f'(\eta))^2 + f(\eta) f''(\eta) + \exp[-\{\beta_1 \theta(\eta) + \beta_2 \phi(\eta)\}](f''''(\eta) - [\beta_1 \theta'(\eta) + \beta_2 \phi'(\eta)] f''(\eta)) + M(E_1 - f'(\eta)) = 0 \tag{12}$$

$$\beta_3 (\theta'(\eta))^2 [1 + \beta_4 \phi(\eta)] + \beta_4 \theta'(\eta) \phi'(\eta) [1 + \beta_3 \theta(\eta)] + \theta''(\eta) [1 + \beta_3 \theta(\eta)] [1 + \beta_4 \phi(\eta)] + \text{Pr} (f(\eta) \theta'(\eta) + \text{Nb} \theta'(\eta) \phi'(\eta) + \text{Nt} (\theta'(\eta))^2 + \text{MEc} [f'(\eta) - E_1]^2 + \frac{4}{3} \text{Rd} [3r(1 + r\theta(\eta))^2 (\theta'(\eta))^2 + (1 + r\theta(\eta))^3 \theta''(\eta)]) = 0 \tag{13}$$

$$\phi''(\eta) + \frac{\text{Nt}}{\text{Nb}} \theta''(\eta) + \text{Sc} [f(\eta) \phi'(\eta) - R \phi(\eta)] = 0 \tag{14}$$

The transformed boundary conditions are rewritten as:

$$\begin{aligned} f'(0) &= 1, & f(0) &= 0, & \theta(0) &= 1, & \phi(0) &= 1 \\ f'(\infty) &\rightarrow 0, & \theta(\infty) &\rightarrow 0, & \phi(\infty) &\rightarrow 0 \end{aligned} \tag{15}$$

In the above system,  $\beta = (\mu_0 \sqrt{2\pi_c}) / p_y$  represents the Casson parameter, that for Newtonian nanofluid, its value tends to infinity whereas for non-Newtonian nanofluid takes small values.  $M = (\sigma B_0^2) / (a \rho_f)$  and  $E_1 = E_0 / (u_w B_0)$  are the magnetic and electric fields parameters.  $\text{Pr} = \mu_0 (c_p) / k_0$  represents the Prandtl number (for human blood  $\text{Pr} \approx 21$ ).  $\text{Nt} = r \Gamma D_B (\rho_f / \mu_0)$  and  $\text{Nb} = (C_w - C_\infty) \Gamma D_B (\rho_f / \mu_0)$  are the thermophoresis and Brownian motion parameters, where  $r = (T_w - T_\infty) / T_\infty$  represents the relative temperature difference through the flow, which has  $r = 0$  for linear radiation.  $\text{Sc} = \mu_0 / (D_B \rho_f)$  and  $\text{Ec} = u_w^2 / [(T_w - T_\infty)(c_p)_f]$  are the Eckert and Schmidt numbers, respectively.  $\text{Rd} = 4 T_\infty^3 \sigma^* / (k_0 \kappa)$  and  $R = R_c / a$  are the radiation and homogeneous chemical reaction parameters, respectively.

Equation (12) at  $\beta_1 = \beta_2 = M = 0$ , and  $\beta \rightarrow \infty$  has an exact solution in the form [40]:

$$f(\eta) = 1 - e^{-\eta} \tag{16}$$

### 2.1 Physical quantities of interest

The most important physical quantities are the skin friction coefficient  $Cf_x$ , Nusselt number  $Nu_x$ , and nanoparticle Sherwood number  $Sh_{x,n}$ . Introducing the dimensionless quantities expressions for  $Cf_x$ ,  $Nu_x$  and  $Sh_{x,n}$  as [34, 39]:

$$\left. \begin{aligned} Cf_x &= \frac{\tau_w}{\rho_f u_w^2} = \frac{\mu_0}{\rho_f u_w^2} \left( \exp[-\{\beta_1 \theta(\eta) + \beta_2 \phi(\eta)\}] + \frac{1}{\beta} \right) \left( \frac{\partial u}{\partial y} \right)_{y=0} = \frac{2}{\sqrt{\text{Re}}} \left( \exp[-\{\beta_1 \theta(0) + \beta_2 \phi(0)\}] + \frac{1}{\beta} \right) f''(0), \\ Nu_x &= \frac{x q_r}{k(T_w - T_\infty)} = -\frac{4}{3} \sqrt{\text{Re}} \text{Rd} \theta'(0), \\ Sh_{x,n} &= \frac{x q_m}{D_B (C_w - C_\infty)} = -\sqrt{\text{Re}} \phi'(0). \end{aligned} \right\} \tag{17}$$

where  $\text{Re} = a x^2 (\rho_f / \mu_0)$  represents the Reynolds number of characteristic velocity and  $q_m = -D_B (\partial C / \partial y)_{y=0}$ .

### 3. Numerical Approach

The steady incompressible two dimensional radiative electro magneto Casson nanofluid flow past a stretching sheet under the influences of the phenomenon of chemical reaction and nonlinear thermal radiation has been formulated. The transformed coupled non-linearly ODEs system (12)-(14) with boundary conditions (15) are solved numerically by the fourth-order Runge-Kutta approach with shooting technique [41] and [42]. For this numerical investigations, the step size  $10^{-2}$  has been chosen and having error tolerance  $10^{-6}$ .



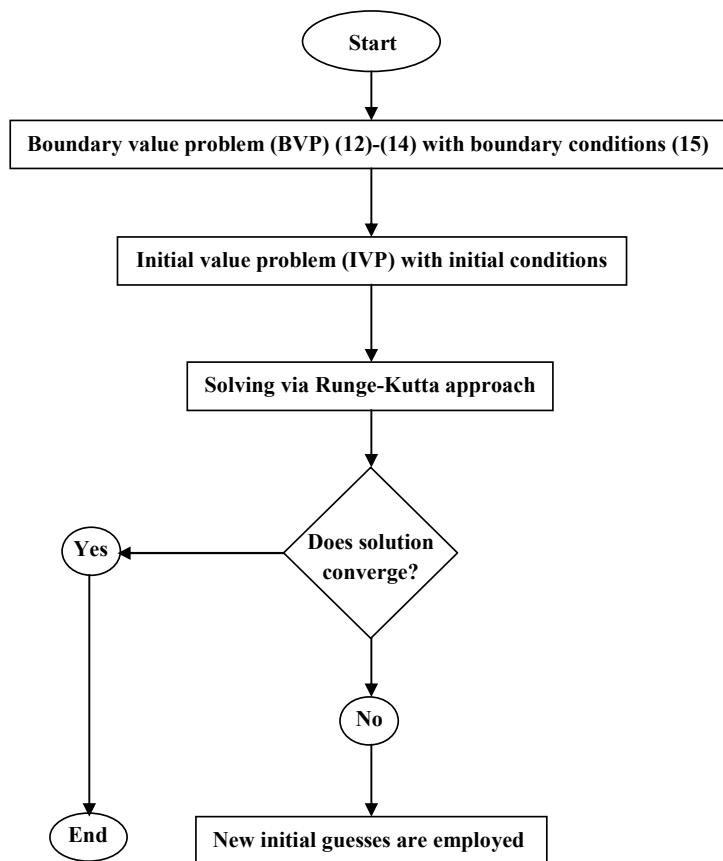


Fig. 2. Flow chart for describing the numerical approach.

The highlighted numerical technique can be outlined as:

- The present physical problem is modeling as a boundary value problem which transformed into initial one.
- Since the constructed coupled non-linear ODEs system (12)-(14) has two second-order equations and one third-order, and then if seven initial conditions available its numerical solution can be obtained. But only four initial conditions in Eq. (15) are given.
- Thence, suitable three initial conditions must be added as  $f''(0) = \varepsilon_1$ ,  $\theta'(0) = \varepsilon_2$  and  $\phi'(0) = \varepsilon_3$  (guesses).
- The physical domain  $[0, \infty]$  is taken as a computational one  $[0, \eta_\infty]$  ( $\eta_\infty = 20$  is chosen).
- Runge-Kutta approach is utilized as well as the numerical solution is obtained.
- The iteration procedure is worked until the convergence condition (the difference between the given boundary conditions in Eq. (15)  $f'(\infty) = \theta(\infty) = \phi(\infty) = 0$  and the computed one is less than  $10^{-6}$ ) is satisfied, otherwise new initial guesses are employed (see Fig. 2).

To validate the present numerical simulation, a comparison is carried out in special case with the exact solution (16) for different values of  $\eta$ .

From the last column in Table 1, a very small error between the present numerical solution and the exact one makes it potential to expand the calculated results.

#### 4. Results and Discussion

The fourth-order Runge-Kutta/shooting technique is used in this numerical simulation to investigate the impact of modulated viscosity/thermal conductivity dependent temperature/nanoparticles concentration parameters on the flow of a radiative electro magneto-Casson nanofluid past a stretching sheet with chemical reaction and nonlinear thermal radiation. Consequently, the present numerical outcomes can be introduced as follows in the next subsection.

Table 1. The values of horizontal nanofluid velocity  $f'(\eta)$  for the exact solution (16) [40] and the present shooting method for different values of  $\eta$  at  $\eta_\infty = 20$ .

$\eta$	Exact solution [40]	Present solution	Error
0.039	0.0386593837529049	0.0386591476413136	$2.3 \times 10^{-7}$
0.157	0.1453678994115584	0.1453660783061044	$1.8 \times 10^{-6}$
0.351	0.2960990090423304	0.2960968776908371	$2.1 \times 10^{-6}$
0.618	0.4612300455246082	0.4612275832395130	$2.4 \times 10^{-6}$
0.954	0.6151551558484238	0.6151515852006927	$3.5 \times 10^{-6}$
1.355	0.7420931647336533	0.7420835325250135	$9.6 \times 10^{-6}$



**Table 2.** Variations of numerical results for  $\sqrt{\text{Re} Cf}$ ,  $-\theta'(0)$  and  $-\phi'(0)$  at various values of  $\beta, \beta_1, \beta_2, \beta_3$  and  $\beta_4$  when  $M = 0.01, Sc = 1, E_1 = Ec = r = Rd = R = Nt = Nb = 0.1$  and  $Pr = 21$  in the present study.

$\beta$	$\beta_1$	$\beta_2$	$\beta_3$	$\beta_4$	$\sqrt{\text{Re} Cf}$	$-\theta'(0)$	$-\phi'(0)$
0.1	0.1	0.1	0.1	0.1	-6.72303	1.19949	0.0785054
0.5					-3.40357	1.16517	0.00736249
1					-2.73838	1.14702	-0.0248463
0.1	0.5	0.1	0.1	0.1	-6.69474	1.19876	0.0779662
	2				-6.63169	1.19743	0.0766127
	5				-6.58773	1.19701	0.07545098
0.1	0.1	0.5	0.1	0.1	-6.66037	1.19886	0.07719682
		2			-6.54464	1.19794	0.07492433
		5			-6.49250	1.19787	0.07424840
0.1	0.1	0.1	0.1	0.1	-6.72303	1.19949	0.07850539
			1		-6.72288	1.08485	0.18033793
			1.75		-6.72277	1.01085	0.24470043
0.1	0.1	0.1	0.1	0.1	-6.72303	1.19949	0.07850539
			1		-6.72281	1.11934	0.14295951
			1.75		-6.72265	1.06046	0.19056094

**Table 3.** Variations of numerical results for  $\sqrt{\text{Re} Cf}$ ,  $-\theta'(0)$  and  $-\phi'(0)$  at various values of  $M, E_1, Ec, R$  and  $Sc$  when  $\beta = \beta_1 = \beta_2 = \beta_3 = \beta_4 = r = Rd = Nt = Nb = 0.1$  and  $Pr = 21$ .

$M$	$E_1$	$Ec$	$R$	$Sc$	$\sqrt{\text{Re} Cf}$	$-\theta'(0)$	$-\phi'(0)$
0.1	0.1	0.1	0.1	0.1	-6.93871	1.18266	0.08958674
0.5					-7.83871	1.11185	0.13691404
0.7					-8.25774	1.07855	0.15955983
0.1	0.1	0.1	0.1	0.1	-6.93871	1.18266	0.08958674
	0.5				-6.69063	1.19437	0.08376979
	0.7				-6.56806	1.19518	0.08360698
0.1	0.1	0.1	0.1	0.1	-6.93871	1.18266	0.08958674
		1.1			-6.93828	1.00763	0.23919509
		1.2			-6.93823	0.99005	0.25423678
0.1	0.1	0.1	0.1	0.1	-6.93871	1.18266	0.08958674
			0.3		-6.93987	1.15812	0.28516306
			0.5		-6.94084	1.13778	0.45535136
0.1	0.1	0.1	0.1	0.25	-6.92794	1.33093	-0.68917003
				0.5	-6.93340	1.26326	-0.34881598
				1	-6.93871	1.18266	0.08958674

**Table 4.** Variations of numerical results for  $\sqrt{\text{Re} Cf}$ ,  $-\theta'(0)$  and  $-\phi'(0)$  at various values of  $r, Rd, Nt$  and  $Nb$  when  $M = 0.01, Sc = 1, \beta = \beta_1 = \beta_2 = \beta_3 = \beta_4 = E_1 = Ec = R = 0.1$  and  $Pr = 21$ .

$r$	$Rd$	$Nt$	$Nb$	$\sqrt{\text{Re} Cf}$	$-\theta'(0)$	$-\phi'(0)$
0.05	0.1	0.1	0.1	-6.72310	1.27279	0.01190467
0.1				-6.72303	1.19949	0.07850539
0.2				-6.72288	1.06750	0.19682817
0.1	0.05	0.1	0.1	-6.72348	1.42548	-0.11090389
	0.1			-6.72303	1.19949	0.07850539
	0.2			-6.72230	0.95499	0.27404153
0.1	0.1	0.1	0.1	-6.72303	1.19949	0.07850539
		0.3		-6.71178	0.98013	-0.76694898
		0.5		-6.70275	0.80082	-1.03301265
0.1	0.1	0.1	0.1	-6.72303	1.19949	0.07850539
			0.3	-6.72640	0.89030	0.64745735
			0.5	-6.72630	0.64069	0.74919090

#### 4.1 Simulation values for $\sqrt{\text{Re} Cf}$ , $-\theta'(0)$ and $-\phi'(0)$

Table 2 shows the numerical changes for  $\sqrt{\text{Re} Cf}$ ,  $-\theta'(0)$  and  $-\phi'(0)$  at different values of  $\beta, \beta_1, \beta_2, \beta_3$  and  $\beta_4$  when  $M = 0.01, Sc = 1, E_1 = Ec = r = Rd = R = Nt = Nb = 0.1$  and  $Pr = 21$ . The discovery revealed that  $\sqrt{\text{Re} Cf}$  is a rising function as the values of  $\beta, \beta_1, \beta_2, \beta_3$  and  $\beta_4$  increase, but  $-\theta'(0)$  is a decreasing function. It is worth noting that when  $\beta, \beta_1$  and  $\beta_2$  increase,  $-\phi'(0)$  is a decreasing function, but when  $\beta_3$  and  $\beta_4$  rise, it is an increasing function. Table 3 presents the numerical values of  $\sqrt{\text{Re} Cf}$ ,  $-\theta'(0)$  and  $-\phi'(0)$  for various values of  $M, E_1, Ec, R$  and  $Sc$  when  $\beta = \beta_1 = \beta_2 = \beta_3 = \beta_4 = r = Rd = Nt = Nb = 0.1$  and  $Pr = 21$ . The numerical results show that raising each of the  $E_1$  and  $Ec$  parameters raises  $\sqrt{\text{Re} Cf}$  and vice versa for  $M, R$  and  $Sc$  parameters. On the other hand,  $-\theta'(0)$  is a decreasing function with rising  $M, Ec, R$  and  $Sc$  parameters and vice versa with  $E_1$ .  $-\phi'(0)$  is also a rising function as  $M, Ec, R$  and  $Sc$  rise, however, it is a decreasing function as  $E_1$  increases. Table 4 illustrates the numerical fluctuation of  $\sqrt{\text{Re} Cf}$ ,  $-\theta'(0)$  and  $-\phi'(0)$  at different values of  $r, Rd, Nt$  and  $Nb$  when  $M = 0.01, Sc = 1, \beta = \beta_1 = \beta_2 = \beta_3 = \beta_4 = E_1 = Ec = R = 0.1$  and  $Pr = 21$ . It is seen that  $\sqrt{\text{Re} Cf}$  is an increasing function when the parameters  $r, Rd$  and  $Nt$  rise, but it is a decreasing function when the parameter  $Nb$  increases, however,  $-\theta'(0)$  is a decreasing function when the parameters  $r, Rd, Nt$  and  $Nb$  increase. Furthermore, as the parameters  $r, Rd$  and  $Nb$  grow,  $-\phi'(0)$  becomes a rising function, but it becomes a decreasing function when the value  $Nt$  increases.



4.2 Evidence and opinions related heat and mass transfer

For the purposes of discussing the effects of the parameters on various flow characteristics, we have assigned the parameters values of  $Pr = 21, M = 0.01, Sc = \beta = 1$  and  $E_1 = Ec = \beta_1 = \beta_2 = \beta_3 = \beta_4 = r = Rd = R = Nt = Nb = 0.1$  except as otherwise mentioned. As seen in Fig. 3, raising the parameter  $\beta$  lowers the fluid velocity at the required data. It is crucial to notice that as the parameter  $\beta$  hits unity, the thickness of the boundary layer of the velocity profiles increases and then becomes thin. Physically, as shown in Fig. 3, the wall velocity decreases while the wall drag force increases. When a larger value of  $\beta$  and a brief flow are introduced into the fluid, the fluid velocity is rapidly slowed. Figs. 4-5 depict the impact of the parameters  $\beta_1, \beta_2, \beta_3$  and  $\beta_4$  on the fluid velocity. The velocity profiles are seen to be decreasing functions, although the boundary layer of the velocity profiles for raising the parameters  $\beta_2$  and  $\beta_4$  is bigger than the boundary layer of the velocity profiles for raising the parameters  $\beta_1$  and  $\beta_3$ .

As illustrated in Fig. 6, increasing the parameter  $\beta$  causes the shear stress  $f''(\eta)$  to be a monotonic function that decreases in region  $0 \leq \eta \leq 2$  and increases in the region  $2 \leq \eta \leq 20$ . The flow can penetrate relatively deeply for a low value of  $\beta$ . When the flow reaches the fluid in the region  $2 \leq \eta \leq 20$ , the shear stress profiles at the wall become larger and expand quickly. It is worth noting that the concavity of the velocity  $f'(\eta)$  and shear stress  $f''(\eta)$  profiles has been shifted from above to below in Figs. 3 and 6.

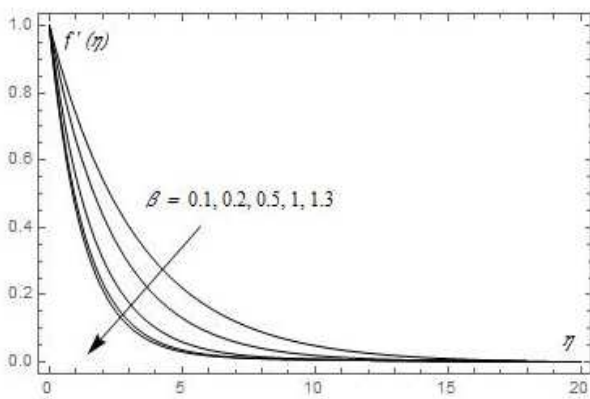


Fig. 3. Impact of  $\beta$  on the velocity profiles.

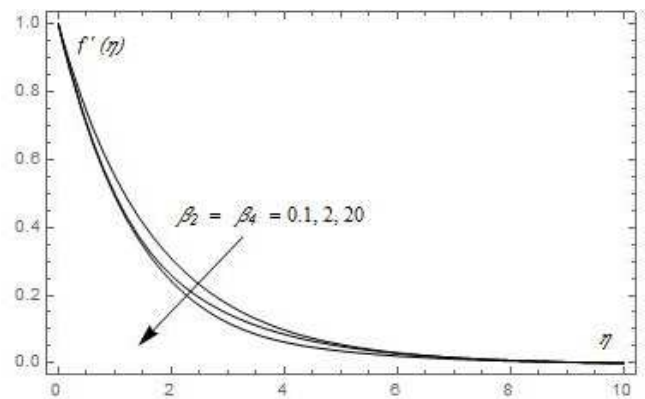


Fig. 4. Impact of  $\beta_2$  and  $\beta_4$  on the velocity profiles.

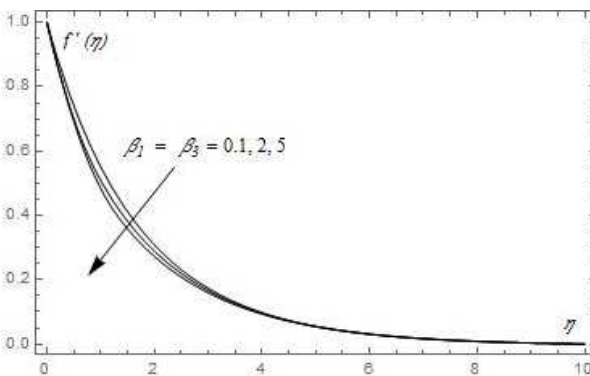


Fig. 5. Impact of  $\beta_1$  and  $\beta_3$  on the velocity profiles.

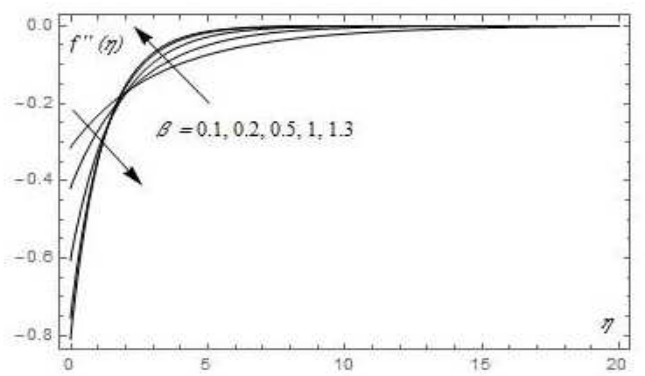


Fig. 6. Impact of  $\beta$  on the shear stress profiles.

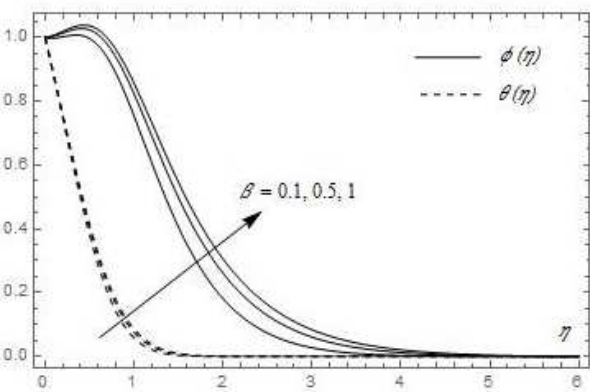


Fig. 7. Impact of  $\beta$  on the temperature and the concentration profiles.

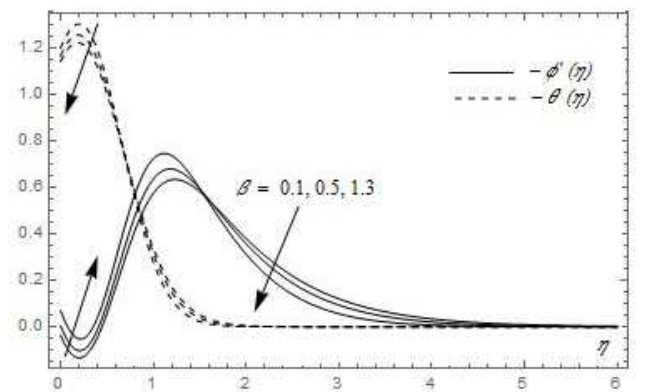


Fig. 8. Impact of  $\beta$  on the heat and mass transfer rate profiles.



The impacts of the specific physical parameters on the temperature profiles, concentration profiles, and heat and mass transfer rates are depicted in Figs 7-22. As the parameter  $\beta$  in Fig. 7 is increased, the temperature and concentration curves both rise. Casson fluidity physically improves temperature and concentration distributions across the flow domain. As can be seen in this figure, the concentration boundary layer appears to be thicker than the thermal boundary layer. However, as shown in Fig. 8, both the heat and mass transfer rate curves are monotonic functions. It is discovered that  $-\theta'(\eta)$  reduces in the region  $0 \leq \eta \leq 0.8$  and grows in the region  $0.8 \leq \eta \leq 6$ . In the opposite direction,  $-\phi'(\eta)$  increases in the region  $0 \leq \eta \leq 1.8$  and decreases in the region  $1.8 \leq \eta \leq 6$ .

The temperature and concentration curves move in opposite directions as the parameters  $E_1$  and  $Ec$  in Fig. 9 are increased, indicating that the temperature curves are growing while the concentration curves are falling. The heat transfer rate curves in Fig. 10 go through two stages as the parameters  $E_1$  and  $Ec$  are increased, decreasing in the range  $0 \leq \eta \leq 1.2$  and slightly growing in the range  $1.2 \leq \eta \leq 6$  whereas mass transfer rate curves have two stages, increasing in range  $0 \leq \eta \leq 1.2$  and decreasing in range  $1.2 \leq \eta \leq 6$ , indicating that both heat and mass transfer rate curves are monotonic functions. The study discovered that as the parameters  $E_1$  and  $M$  in Fig. 11 are increased, the temperature curves climb. Lorentz force, a resistive force, brings this fact together. It is well known that as the magnetic parameter is increased, the velocity profile decreases. Because the application of a transverse magnetic field produces a resistive type force (Lorentz force), which tends to resist the fluid flow and thus reduces its velocity. Furthermore, the thickness of the boundary layer. In contrast, increasing the magnetic parameter decreases the temperature function. Furthermore, higher  $E_1$  and  $M$  values result in more heat and less concentration in the fluid. Whereas the impact of the parameters  $E_1$  and  $M$  in Fig. 12 are minor on the heat transfer rate, they are highly significant on the mass transfer rate.

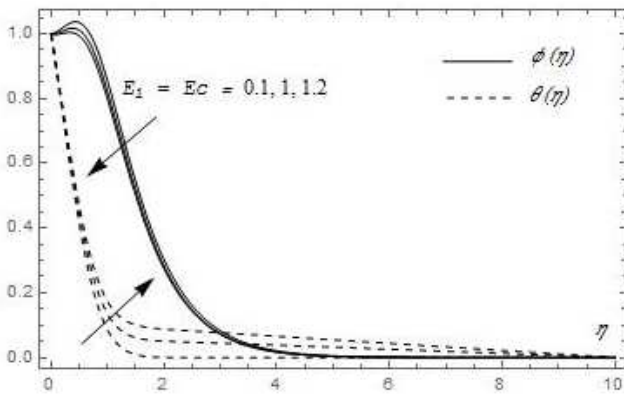


Fig. 9. Impact of  $E_1$  and  $Ec$  on temperature and concentration profiles.

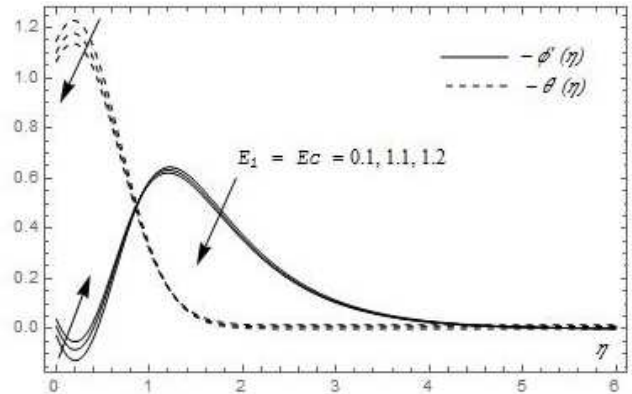


Fig. 10. Impact of  $E_1$  and  $Ec$  on the heat and mass transfer rate profiles.

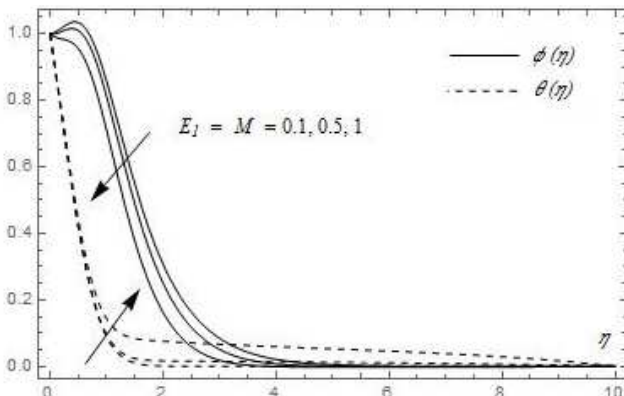


Fig. 11. Impact of  $E_1$  and  $M$  on temperature and concentration profiles.

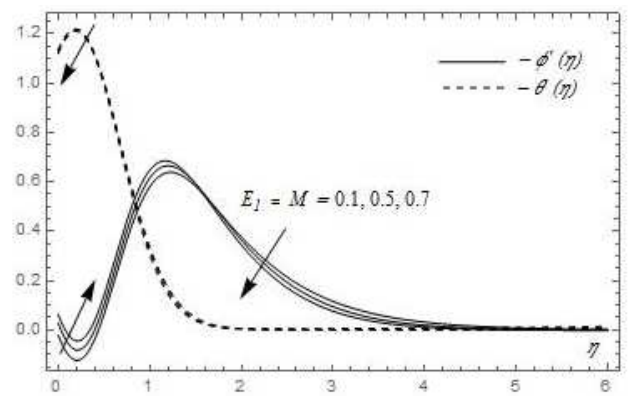


Fig. 12. Impact of  $E_1$  and  $M$  on the heat and mass transfer rate profiles.

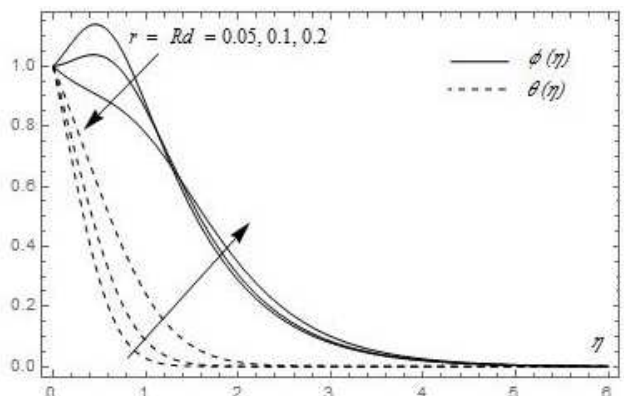


Fig. 13. Impact of  $r$  and  $Rd$  on temperature and concentration profiles.

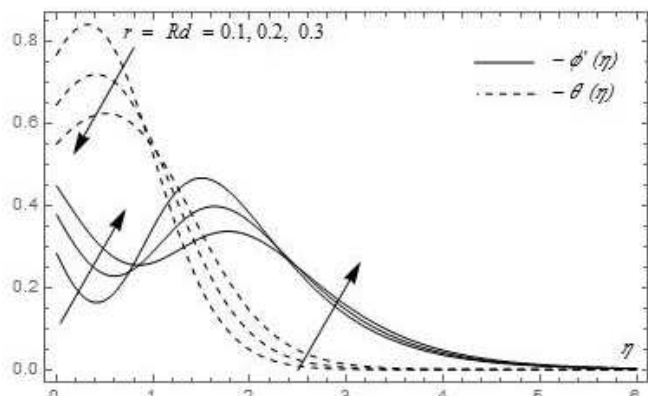


Fig. 14. Impact of  $r$  and  $Rd$  on the heat and mass transfer rate profiles.





Figure 13 depicts the impact of radiation  $Rd$  on the temperature and concentration distributions as nonlinearity increases. The radiation parameter  $Rd$  is a physical measure of the relative importance of thermal radiation transfer to conduction heat transfer. In conclusion, higher values of this quantity indicate that heat radiation is preferred over conduction. As a result, it indicates that more radiative heat energy is being pumped into the system, resulting in an increase in temperature curves. Based on this figure, we can conclude that the function of the nonlinearity parameter  $r$ , which relates to the relative temperature difference inside the flow, on the influence of radiation is fairly clear. It was discovered that the influence of nonlinear radiation is substantially stronger in the case of nonlinearity parameter ( $r \neq 0$ ). Physically, nonlinear radiation will be more successful in temperature-raising applications such as thermal engineering, mechanics, thermal processing, air flow, conditioning systems, and renewable energy. As a consequence, we advocate include the impact of non-linear radiation in future research since it is feasible to obtain more results that are more realistic. Figure 14 also displays the influence of radiation on both heat and mass transfer rate distributions as nonlinearity rises. It is discovered that both the heat and mass transfer rate distributions are monotonic functions, and that the impact of nonlinear radiation is significantly greater.

The temperature and concentration curves move in opposite directions as the parameters  $Sc$  and  $R$  in Fig. 15 are raised, demonstrating that the temperature curves are weakly expanding while the concentration curves are declining with depth of the thermal boundary layer. It has been discovered that as the Schmidt number  $Sc$ , rises, the concentration decreases. This reduces the effects of concentration buoyancy, resulting in a decrease in fluid velocity. Reduced concentration profiles are accompanied by reduced concentration boundary layers. Moreover, the heat and mass transfer rate distributions are both monotonic functions when the parameters  $Sc$  and  $R$  are raised, but the mass transfer rate distributions are considerably larger than the heat transfer rate distributions as seen in Fig. 16.

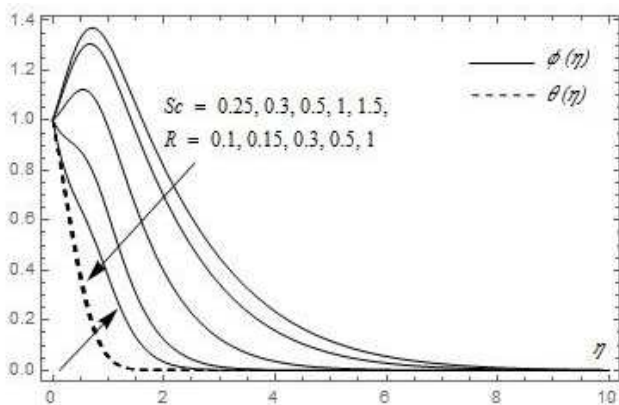


Fig. 15. Impact of  $Sc$  and  $R$  on temperature and concentration profiles.

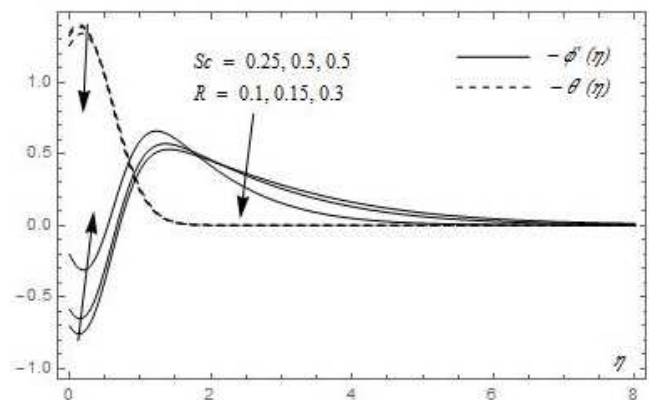


Fig. 16. Impact of  $Sc$  and  $R$  on the heat and mass transfer rate profiles.

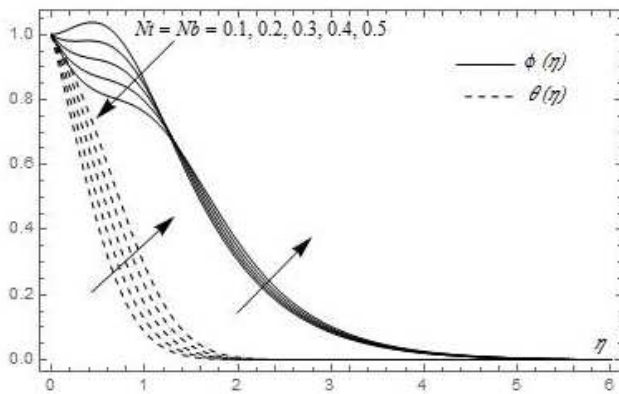


Fig. 17. Impact of  $Nt$  and  $Nb$  on temperature and concentration profiles.

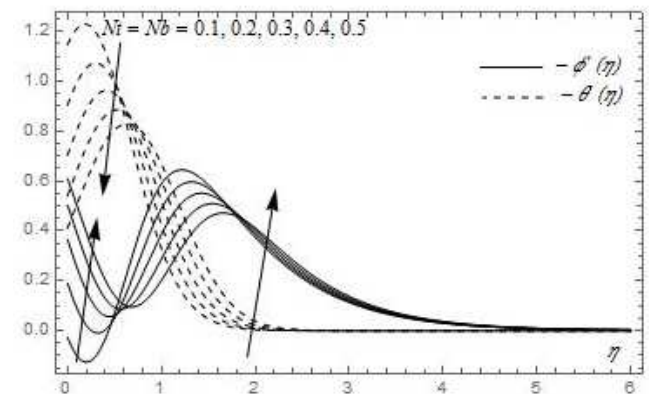


Fig. 18. Impact of  $Nt$  and  $Nb$  on the heat and mass transfer rate profiles.

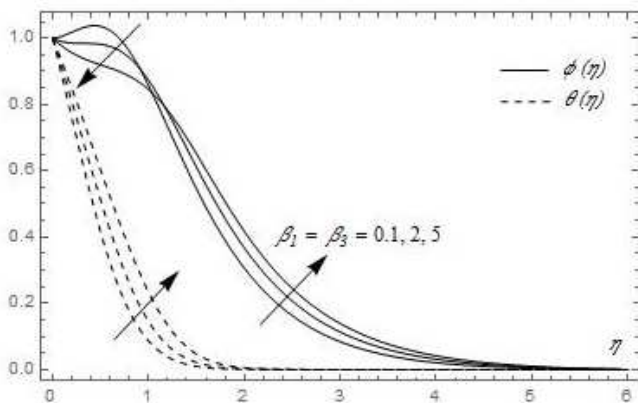


Fig. 19. Impact of  $\beta_1$  and  $\beta_2$  on temperature and concentration profiles.

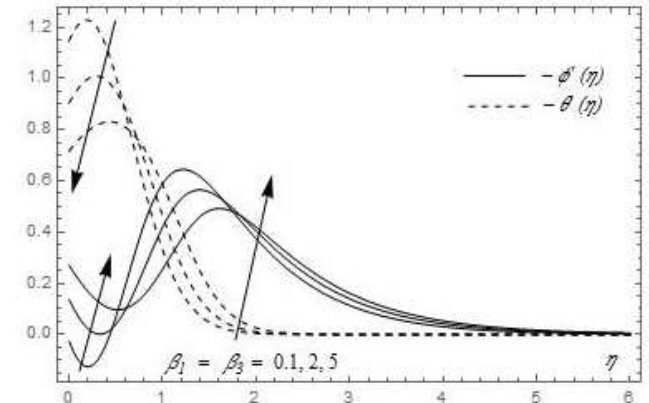


Fig. 20. Impact of  $\beta_1$  and  $\beta_2$  on the heat and mass transfer rate profiles.



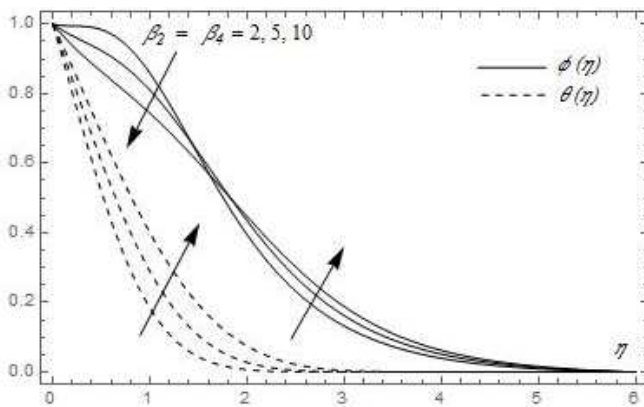


Fig. 21. Impact of  $\beta_2$  and  $\beta_4$  on temperature and concentration profiles.

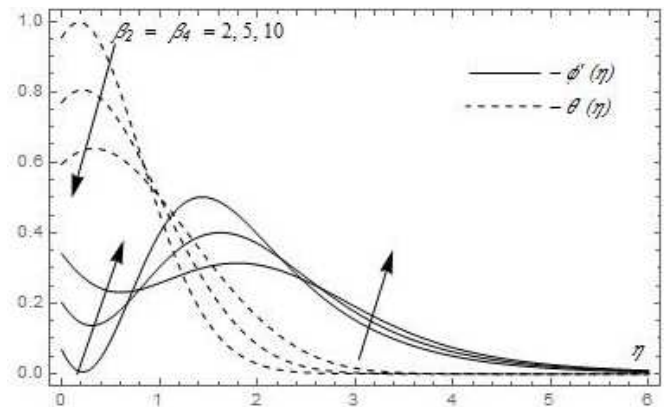


Fig. 22. Impact of  $\beta_2$  and  $\beta_4$  on the heat and mass transfer rate profiles.

The parameters  $Nt$  and  $Nb$ , as shown in Figs 17-18, have a significant effect on the temperature, concentration, heat, and mass transfer rate distributions. Whereas the thermal boundary layers of temperature distributions grow uniformly as the parameters  $Nt$  and  $Nb$  increase, the boundary layers of concentration distributions fall uniformly in the range  $0 \leq \eta \leq 1.4$  and increase in the range  $1.4 \leq \eta \leq 6$ . On the other hand, both the heat and mass transfer rate distributions are discovered to be monotone functions. The heat transfer rate distributions, for example, exhibit thicker thermal boundary layers in the range  $0 \leq \eta \leq 0.7$  than in the region  $0.7 \leq \eta \leq 6$ . Furthermore, the mass transfer rate distributions have three stages: in the first stage  $0 \leq \eta \leq 0.6$  the mass transfer rate distributions increase with increasing in the parameters  $Nt$  and  $Nb$ ; it is noted that in this region, the thermal boundary layer gradually decreases; in the second stage  $0.6 \leq \eta \leq 1.8$ , the mass transfer rate distributions decrease; and in the third stage  $1.8 \leq \eta \leq 6$ , the mass transfer rate distributions increase but with thinness of the thermal boundary layers.

Furthermore, Figs. 19 and 20 show the effect of  $\beta_1$  and  $\beta_3$  on temperature, concentration, heat, and mass transfer rate profiles at various data points. As the parameters  $\beta_1$  and  $\beta_3$  rise, the thermal boundary layers of temperature distributions expand evenly, whereas the boundary layers of concentration distributions decline uniformly in the range  $0 \leq \eta \leq 1.4$  and increase in the range  $1.4 \leq \eta \leq 6$ . As seen in Fig. 20, it has been revealed that the parameters  $\beta_1$  and  $\beta_3$  have a significant influence on both the heat and mass transfer rate distributions and are monotone functions. The heat transfer rate distributions, for particular, show larger thermal boundary layers in range  $0 \leq \eta \leq 0.8$  than in the region range  $0.8 \leq \eta \leq 6$ . Further, the mass transfer rate distribution in Fig. 20 also has three phases just like in Fig. 18.

Finally, when the parameters  $\beta_2$  and  $\beta_4$  in Fig. 21 increase, the thermal boundary layers of temperature distributions grow consistently, but the boundary layers of concentration distributions fall uniformly, as seen in Fig. 19. As given in Fig. 22, the parameters  $\beta_2$  and  $\beta_4$  have a huge effect on both the heat and mass transfer rate distributions, and both distributions are monotone functions, as seen in Fig. 20.

#### 4.3 Future work

The nanoparticles concentration can be modelled by the two-scale fractal fractional dimensions [43, 44] and a fractal-fractional model can take into account the effects of nanoparticles' size and distribution, and the unsmooth boundary, see for examples, Refs. [45-51].

## 5. Conclusion

In this article, the impacts of a modulated viscosity/thermal conductivity dependent temperature/nanoparticles concentration parameter on the flow of a radiative electromagneto-Casson nanofluid past a stretching sheet under the impacts of chemical reaction and nonlinear thermal radiation were utilized in order to enrich the nanofluid flow. The transformed two-dimensional ODEs have been attained numerically via a reliable and proficient approach namely the fourth-order Runge-Kutta/shooting technique. Comparison table, in special case, between the exact solution and the present numerical outcomes represented a good agreement. The impacts of operating parameters on concentration, velocity, and temperature profiles were explained and examined through tables and graphs. The highlighted outcomes can be concluded as:

- The parameters  $\beta_1, \beta_2, \beta_3, \beta_4, r, Rd, Nt$  and  $Nb$  have extremely high efficacy on each of the functions  $\theta(\eta), \phi(\eta), -\theta'(\eta)$  and  $-\phi'(\eta)$ . Temperature, concentration, heat, and mass transfer rate profiles are affected by the thickness of the thermal boundary layers.
- For the physical parameters investigated in this study, the profiles of heat and mass transfer rate are monotonic functions.
- When the parameters,  $\beta, \beta_1, \beta_2, \beta_3, \beta_4, r, Rd, E_1, Ec$  and  $Nt$  increase,  $\sqrt{Re}Cf$  increases, but it decreases when the parameters  $M, R, Sc$  and  $Nb$  increase. Except for the parameter  $E_1$  and  $-\theta'(\eta)$  drops as the physical parameters grow.  $-\phi'(\eta)$  is a decreasing function with rises in the parameters,  $\beta, \beta_1, \beta_2, E_1$  and  $Nt$  and vice versa for the remaining parameters.
- In the case of Casson fluid, the parameters  $\beta_1, \beta_2, \beta_3, \beta_4, r, Rd, E_1, M, Nt$  and  $Nb$  all improve the temperature field and increase the thickness of the thermal function's boundary layer, but they decrease heat transfer rates in the previous inducing region while increasing them in the left other region, as shown in the graphs. Because of their widespread use in medical applications and chemical industrial engineering, these characteristics have received a lot of attention
- It is worth noting that the parameters  $\beta, M, E_1, Ec, Sc$  and  $R$  have a modest influence on  $-\theta'(\eta)$ , whereas the parameter  $\beta$  has an attractive effect on the fluid's velocity.

## Author Contributions

J.H. He planned the physical problem; N.S. Elgazery proposed and developed the mathematical modeling; K. Elagamy applied the numerical approach; N.Y. Abd Elazem plotted the figures, analyzed the numerical outcomes. The manuscript was written



through the contribution of all authors. All authors contributed to the writing of the manuscript. The final version of the article was reviewed by all authors, who also gave their approval.

### Acknowledgments

The reviewers' insightful observations, supportive remarks, and helpful recommendations to enhance the original article are all greatly appreciated by the authors.

### Conflict of Interest

Regarding the research, writing, and/or publication of this work, the authors declared that there were no potential conflicts of interest.

### Funding

The authors got no financial support of the authorship, work, and/or publication of the current manuscript.

### Data Availability Statements

The datasets generated and/or analyzed during the current study are available from the corresponding author on reasonable request.

### Nomenclature

#### Roman Symbols

$V = (u, v)$	nanofluid velocities in the directions $(x, y)$
$T$	nanofluid temperature
$C$	nanoparticles concentration
$J$	electrical conducting density (joule current)
$\sigma$	electrical conductivity
$E = (0, 0, -E_0)$	uniform electric field vector of strength $E_0$
$B = (0, B_0, 0)$	uniform magnetic field vector of strength $B_0$
$p_y$	yield stress
$e_{ij}$	the $(i, j)^{th}$ component of the deformation rate
$c_p$	specific heat at constant pressure
$k, k_0$	variable and constant thermal conductivity
$D_B, D_T$	Brownian and thermophoresis diffusion coefficients
$q_r$	thermal radiative heat flux
$Pr$	Prandtl number
$Rd$	radiation parameter
$R$	homogeneous chemical reaction parameter
$Ec$	Eckert number
$Sc$	Schmidt number
$r$	relative temperature difference through the flow
$M, E_1$	magnetic field and electric field parameters
$u_w = ax$	stretching velocity
$Nb, Nt$	Brownian motion and thermophoresis parameters
$Cf$	local skin friction coefficient
$Nu_x, Sh_{x,n}$	Nusselt and nanoparticle Sherwood numbers
$a$	constant
$q_1, q_2, q_3, q_4$	dimensionless coefficients
$f(\eta)$	dimensionless velocity

#### Greek Symbols

$\tau_{ij}$	stress tensor
$\Gamma = (\rho c_p)_s / (\rho c_p)_f$	ratio between the effective heat capacity of the nanoparticles and heat capacity of the base fluid
$\rho_f$	nanofluid density
$\kappa$	mean absorption coefficient
$\sigma^*$	Stefan-Boltzman constant



$\mu, \mu_0$	variable and constant viscosity
$\theta(\eta), \phi(\eta)$	dimensionless temperature and nanoparticles concentration
$\eta$	similarity variable
$\eta_\infty$	the upper limit of the independent variable
$\psi$	stream function
$\beta_1, \beta_3$	viscosity and thermal conductivity temperature variation parameters
$\beta_2, \beta_4$	viscosity and thermal conductivity nanoparticles concentration variation parameters
$\beta$	Casson parameter

### Subscripts/Superscripts

$f$	base fluid
$s$	nano-solid-particles
$w$	condition on the surface
$\infty$	far field
'	differentiation with respect to $\eta$

### References


- [1] Al-Khaled, K., Khan, S.U., Thermal aspects of casson nanofluid with gyrotactic microorganisms, temperature-dependent viscosity, and variable thermal conductivity: Bio-technology and thermal applications, *Inventions*, 5(3), 2020, 1–14.
- [2] Gbadeyan, J.A., Titiloye, E.O., Adeosun, A.T., Effect of variable thermal conductivity and viscosity on Casson nanofluid flow with convective heating and velocity slip, *Heliyon*, 6(1), 2020, e03076.
- [3] Fung, Y., *Biodynamics: Circulation*, Springer-Verlag, New York, 1984.
- [4] Nakamura, M., Sawada, T., Numerical study on the flow of a non-Newtonian fluid through an axisymmetric stenosis, *Journal of Biomechanical Engineering*, 110(2), 1988, 137–143.
- [5] Haemmerich, D., Wright, A.W., Mahvi, D.M., Lee, F.T., Webster, J.G., Hepatic bipolar radiofrequency ablation creates coagulation zones close to blood vessels: a finite element study, *Medical & Biological Engineering & Computing*, 41(3), 2003, 317–323.
- [6] Casson, N., *A flow equation for pigment-oil suspensions of the printing ink type*, In: Mill, C.C., Ed., *Rheology of Disperse Systems*, Pergamon Press, Oxford, 1959.
- [7] Giresha, B.J., Kumar, P.B.S., Mahanthesh, B.S., Shehzad, A., Rauf, A., Nonlinear 3D flow of Casson-Carreau fluids with homogeneous – heterogeneous reactions: A comparative study, *Results in Physics*, 7, 2017, 2762–2770.
- [8] Walawender, W.P., Chen, T.Y., Cala, D.F., An approximate Casson fluid model for tube flow of blood, *Biorheology*, 12(2), 1975, 111–119.
- [9] Srivastava, L.M., Srivastava, V.P., Peristaltic transport of blood: Casson model-II, *Journal of Biomechanics*, 17(11), 1984, 821–829.
- [10] Dash, R.K., Mehta, K.N., Jayaraman, G., Casson fluid flow in a pipe filled with a homogeneous porous medium, *International Journal of Engineering Science*, 34(10), 199, 1145–1156.
- [11] Eldabe, N.T.M., Saddeck, G., El-Sayed, A.F., Heat transfer of MHD non-Newtonian Casson fluid flow between two rotating cylinders, *Mechanics and Mechanical Engineering*, 5(2), 2001, 237–251.
- [12] Mernone, A.V., Mazumdar, J.N., Lucas, S.K., A mathematical study of peristaltic transport of a Casson fluid, *Mathematical and Computer Modelling*, 35(7-8), 2002, 895–912.
- [13] Mustafa, M., Hayat, T., Pop, I., Aziz, A., Unsteady boundary layer flow of a Casson fluid due to an impulsively started moving flat plate, *Heat Transfer Research*, 40(6), 2011, 563–576.
- [14] Shehzad, S.A., Hayat, T., Qasim, M., Asghar, S., Effects of mass transfer on MHD flow of Casson fluid with chemical reaction and suction, *Brazilian Journal of Chemical Engineering*, 30, 2013, 187–195.
- [15] Hayat, T., Asad, S., Alsaedi, A., Flow of Casson fluid with nanoparticles, *Applied Mathematics and Mechanics*, 37(4), 2001, 459–470.
- [16] Ghadikolaei, S.S., Hosseinzadeh, K., Ganji, D.D., Jafari, B., Nonlinear thermal radiation effect on magneto Casson nanofluid flow with Joule heating effect over an inclined porous stretching sheet, *Case Studies in Thermal Engineering*, 12, 2018, 176–187.
- [17] Aman, S., Zokri, S.M., Ismail, Z., Salleh, M.Z., Khan, I., Effect of MHD and porosity on exact solutions and flow of a hybrid casson-nanofluid, *Journal of Advanced Research in Fluid Mechanics and Thermal Sciences*, 44(1), 2018, 131–139.
- [18] Siddiqua, S., Begum, N., Hossain, M.A., Shoaib, M., Reddy Gorla, R.S., Radiative heat transfer analysis of non-Newtonian dusty Casson heat fluid flow along a complex wavy surface, *Numer. Heat Transf. Part A Appl.*, 73 (4), 2018, 209–221.
- [19] Elgazery, N.S., Flow of non-Newtonian magneto-fluid with gold and alumina nanoparticles through a non-Darcian porous medium, *Journal of the Egyptian Mathematical Society*, 27(1), 2019, 1–25.
- [20] Hady, F.M., Mahdy, A., Mohamed, R.A., Ahmed, S.E., Abo-zaid, O.A., Unsteady natural convection flow of a dusty non-Newtonian Casson fluid along a vertical wavy plate: numerical approach, *Journal of the Brazilian Society of Mechanical Sciences and Engineering*, 41(11), 2019, 1–20.
- [21] Akolade, M.T., Tijani, Y.O., A comparative study of three dimensional flow of Casson-Williamson nanofluids past a rigid plate: Spectral quasi-linearization approach, *Partial Differential Equations in Applied Mathematics*, 4, 2021, 100108.
- [22] Elelmy, A.F., Elgazery, N.S., Ellahi, R., Blood flow of MHD non-Newtonian nanofluid with heat transfer and slip effects: Application of bacterial growth in heart valve, *International Journal of Numerical Methods for Heat & Fluid Flow*, 30(11), 2020, 4883–4908.
- [23] Usman, M., Gul, T., A., Khan, Alsubie, A., Zaka, M., Electromagnetic couple stress film flow of hybrid nanofluid over an unsteady rotating disc, *International Communications in Heat and Mass Transfer*, 127, 2021, 105562.
- [24] Varun Kumar, R.S., Gunderi Dhananjaya, P., Naveen Kumar, R.R., Punith Gowda, J., Prasannakumara, B.C., Modeling and theoretical investigation on Casson nanofluid flow over a curved stretching surface with the influence of magnetic field and chemical reaction, *International Journal for Computational Methods in Engineering Science and Mechanics*, 23(1), 2022, 12–19.
- [25] Venkata Ramudu, A.C., Anantha Kumar, K., Sugunamma, V., Sandeep, N., Impact of Soret and Dufour on MHD Casson fluid flow past a stretching surface with convective-diffusive conditions, *Journal of Thermal Analysis and Calorimetry*, 147(3), 2022, 2653–2663.
- [26] Elgazery, N.S., Hassan, M.A., The effects of variable fluid properties and magnetic field on the flow of non-Newtonian fluid film on an unsteady stretching sheet through a porous medium, *Communications in Numerical Methods in Engineering*, 24(12), 2008, 2113–2129.
- [27] Elgazery, N.S., El-Sayed, M.F., Effects of magneto-Marangoni convection with variable properties on non-Newtonian biviscosity fluid over stretching sheet in porous medium, *Journal of Porous Media*, 17(10), 2014, 901–912.
- [28] Elgazery, N.S., Numerical simulation for biviscosity fluid flow through a porous medium under the effects of variable properties, *Special Topics and Reviews in Porous Media*, 3(1), 2012, 1–11.
- [29] Animasaun, I.L., Effects of thermophoresis, variable viscosity and thermal conductivity on free convective heat and mass transfer of non-darcian MHD dissipative Casson fluid flow with suction and nth order of chemical reaction, *Journal of the Nigerian Mathematical Society*, 34(1), 2015, 11–31.
- [30] El-Aziz, M.A., Afify, A.A., Effects of Variable Thermal Conductivity with Thermal Radiation on MHD Flow and Heat Transfer of Casson Liquid Film Over an Unsteady Stretching Surface, *Brazilian Journal of Physics*, 46(5), 2001, 516–525.
- [31] Nawaz, M., Naz, R., Awais, M., Magneto-hydrodynamic axisymmetric flow of Casson fluid with variable thermal conductivity and free stream,




*Alexandria Engineering Journal*, 57(3), 2018, 2043–2050.


- [32] Sohail, M., Shah, Z., Tassaddiq, A., Kumam, P., Roy, P., Entropy generation in MHD Casson fluid flow with variable heat conductance and thermal conductivity over non-linear bi-directional stretching surface, *Scientific Reports*, 10(1), 2020, 1–16.
- [33] Bisht, A., Sharma, R., Non-similar solution of Casson nanofluid with variable viscosity and variable thermal conductivity, *International Journal of Numerical Methods for Heat & Fluid Flow*, 22(7), 2020, 3919–3938.
- [34] Elgazery, N.S., Elelmy, A.F., Multiple solutions for non-Newtonian nanofluid flow over a stretching sheet with nonlinear thermal radiation: Application in transdermal drug delivery, *Pramana*, 94(1), 2020, 8–94.
- [35] Kumar, K., Chauhan, P.R., Kumar, R., Bharj, R.S., Irreversibility analysis in Al<sub>2</sub>O<sub>3</sub>-water nanofluid flow with variable property, *Facta Universitatis, Series: Mechanical Engineering*, 20(3), 2022, 503–518.
- [36] Feijó, B.C., Pavlovic, A., Rocha, L.A.O., Isoldi, L.A., Lorente, S., dos Santos, E.D., Geometrical investigation of microchannel with two trapezoidal blocks subjected to laminar convective flows with and without boiling, *Reports in Mechanical Engineering*, 3(1), 2022, 20–36.
- [37] Aliy, G., Kishan, N., Effect of Electric Field on MHD Flow and Heat Transfer Characteristics of Williamson Nanofluid over a Heated Surface with Variable Thickness, *OHAM Solution*, 30(1), 2019, 1–23.
- [38] Bhargava, R., Chandra, H., Numerical simulation of MHD boundary layer flow and heat transfer over a nonlinear stretching sheet in the porous medium with viscous dissipation using hybrid approach, *arXiv:1711.03579 [physics.flu-dyn]*.
- [39] Ahmed, S.E., Mansour, M.A., Mahdy, A. Mohamed, S.S., Entropy generation due to double diffusive convective flow of Casson fluids over nonlinearity stretching sheets with slip conditions, *Engineering Science and Technology, an International Journal*, 20, 2017, 1553–1562.
- [40] Crane, L.J., Flow past a stretching plate, *Zeitschrift für Angewandte Mathematik und Physik*, 21(4), 1970, 645–647.
- [41] Elgazery, N.S., Nanofluids flow over a permeable unsteady stretching surface with non-uniform heat source/sink in the presence of inclined magnetic field, *Journal of the Egyptian Mathematical Society*, 27(1), 2019, 1–26.
- [42] Afify, A.A., Elgazery, N.S., Lie group analysis for the effects of chemical reaction on MHD stagnation-point flow of heat and mass transfer towards a heated porous stretching sheet with suction or injection, *Nonlinear Analysis: Modelling and Control*, 17(1), 2012, 1–15.
- [43] Qian, M.Y., He, J.H., Two-scale thermal science for modern life: Making the Impossible Possible, *Thermal Science*, 26(3), 2022, 2409–2412.
- [44] He, J.H., Seeing with a single scale is always unbelieving: From magic to two-scale fractal, *Thermal Science*, 25(2), 2021, 1217–1219
- [45] Liu, F.J., Zhang, T., He, C.H., Tian, D., Thermal oscillation arising in a heat shock of a porous hierarchy and its application, *Facta Universitatis Series Mechanical Engineering*, 20(3), 2022, 633–645.
- [46] Xue, R.J., Liu, F.J., A Fractional model and its application to heat prevention coating with cocoon-like hierarchy, *Thermal Science*, 26(3), 2022, 2493–2498.
- [47] He, C.H., A variational principle for a fractal nano/microelectromechanical (N/MEMS) system, *International Journal of Numerical Methods for Heat & Fluid Flow*, 2022, DOI: 10.1108/HFF-03-2022-0191.
- [48] Wang, K.L., Novel analytical approach to modified fractal gas dynamics model with the variable coefficients, *ZAMM Zeitschrift für Angewandte Mathematik und Mechanik*, 2023, DOI: 10.1002/zamm.202100391.
- [49] Wang, K.L., Wei, C.F., Fractal soliton solutions for the fractal-fractional shallow water wave equation arising in ocean engineering, *Alexandria Engineering Journal*, 65, 2023, 859–865.
- [50] Li, Z.Y., Wang, M.C., Wang, Y.L., Solving a class of variable order nonlinear fractional integral differential equations by using reproducing kernel function, *AIMS Mathematics*, 7(7), 2022, 12935–12951
- [51] Li, Z.Y., Chen, Q.T., Wang, Y.L., Li, X.Y., Solving two-sided fractional super-diffusive partial differential equations with variable coefficients in a class of new reproducing kernel spaces, *Fractal and Fractional*, 6(9), 2022, 492.

## ORCID iD

Ji-Huan He  <https://orcid.org/0000-0002-1636-0559>

Nasser S. Elgazery  <https://orcid.org/0000-0003-4691-2526>

Khaled Elagamy  <https://orcid.org/0000-0001-8216-3935>

Nader Y. Abd Elazem  <https://orcid.org/0000-0003-4625-0358>



© 2023 Shahid Chamran University of Ahvaz, Ahvaz, Iran. This article is an open access article distributed under the terms and conditions of the Creative Commons Attribution-NonCommercial 4.0 International (CC BY-NC 4.0 license) (<http://creativecommons.org/licenses/by-nc/4.0/>).

**How to cite this article:** He J.H., Elgazery N.S., Elagamy K., Abd Elazem N.Y. Efficacy of a modulated viscosity-dependent temperature/nanoparticles concentration parameter on a nonlinear radiative electromagneto-nanofluid flow along an elongated stretching sheet, *J. Appl. Comput. Mech.*, 9(3), 2023, 848–860. <https://doi.org/10.22055/jacm.2023.42294.3905>

**Publisher's Note** Shahid Chamran University of Ahvaz remains neutral with regard to jurisdictional claims in published maps and institutional affiliations.

